RESEARCH ARTICLE | SEPTEMBER 10 2024

Intensifying interfacial oscillations in falling film flows over rectangular corrugations

A. Düll ; A. Cros-Le Lagadec ; J. Buchmüller ; T. Häber ; C. Ateş ; M. Börnhorst

Physics of Fluids 36, 092107 (2024)
https://doi.org/10.1063/5.0222760

Physics of Fluids ARTICLE pubs.aip.org/aip/pof

Intensifying interfacial oscillations in falling film flows over rectangular corrugations

Cite as: Phys. Fluids **36**, 092107 (2024); doi: 10.1063/5.0222760
Submitted: 10 June 2024 · Accepted: 23 August 2024 ·
Published Online: 10 September 2024

A. Düll,[1] A. Cros-Le Lagadec,[1] J. Buchmüller,[1] T. Häber,[2,a)] C. Ateş,[3] and M. Börnhorst[4,a)]

AFFILIATIONS

[1]Institute for Chemical Technology and Polymer Chemistry, Karlsruhe Institute of Technology (KIT), Engesserstraße 20, 76131 Karlsruhe, Germany
[2]Institute of Catalysis Research and Technology, Karlsruhe Institute of Technology (KIT), Hermann-von-Helmholtz-Platz 1, 76344 Eggenstein-Leopoldshafen, Germany
[3]Institute of Thermal Turbomachinery, Karlsruhe Institute of Technology (KIT), Kaiserstraße 12, 76131 Karlsruhe, Germany
[4]Institute of Reaction Engineering and Catalysis, TU Dortmund University, Emil-Figge-Straße 66, 44227 Dortmund, Germany

[a)]**Authors to whom correspondence should be addressed:** thomas.haeber@kit.edu and marion.boernhorst@tu-dortmund.de

ABSTRACT

Unsteady film flows play an important role in intensifying heat and mass transfer processes, with applications, e.g., in falling film absorbers or reactors. In this context, the influence of surface structure modification on the wave dynamics of falling film flows is experimentally investigated based on localized film thickness time series data. Arrays of rectangular ridges oriented perpendicular to the main flow direction are considered, and an optimum ridge distance is identified, at which particularly strong interfacial oscillations are induced in the falling film. These potentially result from the interaction of the flow with a statically deformed base film under resonance-like conditions. The transient destabilization is amplified in the case of narrow ridge sizes, where inertia-driven flow features are particularly pronounced. With regard to mass transfer applications, the structure-induced increase in gas–liquid interfacial area may be of secondary importance compared to changes in internal flow conditions.

I. INTRODUCTION

Falling film flows are ubiquitous in nature, where they can be observed in many biological and geophysical systems.[1–3] They are also present in a variety of technical and industrial applications.[4] For instance, the behavior of falling films plays an important role in coating processes,[5–10] and the associated heat transfer characteristics determine the efficiency of falling film evaporators. The latter are commonly used in cryogenic air separation units,[11,12] for seawater desalination[13,14] as well as for the recycling of black liquor in pulp mills[15] and the concentration of fruit juice[16] or dairy products.[17] In the chemical industry, falling film reactors have proven to be well suited for strongly exothermic gas–liquid reactions such as sulfonations or chlorinations.[18,19] Furthermore, falling film absorbers find frequent application in absorption refrigeration systems[20,21] or the production of hydrochloric acid (HCl),[22] and have been widely utilized for the investigation of sulfur dioxide (SO_2)[23,24] or carbon dioxide (CO_2)[25–31] absorption. In a more general context, insight gained from the investigation of falling film flow configurations can be employed for the design and optimization of packing materials in absorption or distillation columns.[32–37]

In many of the technical applications previously mentioned, the surface over which the liquid film flows is not smooth but structured. With regard to the heat and mass transfer applications motivating this study, several authors have demonstrated the enhancing effect of two-dimensional, periodic surface structuring on the heat and mass transfer characteristics of falling film flows.[35,38–41] This is mainly attributed to an increased gas–liquid interfacial area and liquid residence time,[42] as well as to the formation of internal recirculation zones.[43] Other works report an insignificant or even adverse impact,[44,45] which can result from unfavorable changes in the mean film thickness and liquid velocity[46] in the case of improperly chosen structure geometries.[45] In this context, the potential of surface structure optimization was highlighted by Davies and Warner.[35] Analyzing a stepwise corrugated surface, they found the strongest mass transport enhancement at an intermediate structure distance-to-height ratio of about five, which they attributed to the interference of vortices forming in the vicinity of two subsequent

structure elements. While the existence of such an optimum structure distance was also speculated by Lu *et al.*,[40] neither of the two works conducted a quantitative analysis of the underlying hydrodynamics. Thus, in order to contribute to such optimization efforts, this study focuses on the structure-induced wave dynamics of falling films under flow conditions relevant to heat and mass transfer applications. Previous hydrodynamic analyses were often conducted at relatively low Reynolds numbers and focused on the structure-induced surface deformation under steady flow conditions. Findings most relevant to this study are briefly outlined below, although the reader is directed to the reviews by Aksel and Schörner[47] and Craster and Matar[1] for a more comprehensive view.

For Stokes flow over a single mound or trench, the evolution of capillary features, e.g., capillary ridges or depressions, was predicted in the vicinity of the obstacles.[48] This surface deformation is strongly affected by the presence of inertia forces.[3] In the case of isolated step geometries, an increase in Reynolds number results in the eventual disappearance of the capillary features.[5] Simultaneously, liquid overshoot in the cross-stream direction leads to the formation and growth of a new, inertia-controlled ridge downstream of a step-out.[5] For a periodic array of two-dimensional structure elements, resonance interaction between the free surface and wall corrugation was predicted in theoretical analyses considering inertia forces.[49–51] In the case of finite corrugation heights, the resonant Reynolds number determined by linear theory[49,50,52] marks the onset of a parametric region characterized by a particularly strong amplification of the steady free surface.[53] A corrugation wavelength of a few millimeters was predicted, where the resonance effect is most pronounced.[49,50,52] The static surface deformation has a significant impact on the dynamic properties of the falling film flow, as traveling disturbances, which can manifest as surface oscillations or traveling waves, continuously interact with the underlying base flow.[53,54] At higher Reynolds numbers, the evolution of steady three-dimensional flow patterns is observed when the distortion of the two-dimensional base flow reaches a maximum steepness at the peak of the nonlinear resonance curve.[53,54] The occurrence of such three-dimensional patterns results in flow stabilization and suppression of traveling waves.[53,55]

The present study complements the previously outlined hydrodynamic analyses by focusing on the dynamic aspects of falling film flows on structured surfaces. This is directly relevant to heat and mass transfer applications, as significantly higher heat and mass transfer rates are achieved under unsteady flow conditions compared to steady ones.[38,39,55] In this context, it is of particular interest to determine whether the static resonance-like effects described above are reflected in the time-oscillatory surface deformation. To this end, falling film flows over arrays of rectangular ridges with systematically varied structure distance and height are experimentally investigated at different Reynolds numbers and plate inclination angles. After establishing operational limits for the individual structure geometries from a practical and methodological perspective, locally recorded film thickness time series are used to characterize the rather chaotic nature of the free-surface dynamics. Emphasis is placed on identifying surface structures that induce a particularly strong oscillatory behavior, as these geometries may be of interest for future structure optimization efforts. In an outlook, potential implications for mass transfer applications are derived from the hydrodynamic results.

The remaining article is organized as follows: The experimental setup and data evaluation procedure are outlined in Sec. II. The experimental results are presented and discussed in Sec. III and the main conclusions are summarized in Sec. IV.

II. EXPERIMENTAL SETUP AND METHODOLOGY

A. Falling film test rig

The experimental test rig is schematically shown in Fig. 1. The working fluid is pumped from the main supply reservoir into a settling chamber by means of a micro-gear pump (LAB-ZP-9, Gather Industries). In addition to a check valve, a filter (20 μm mesh size) is installed in the feed line to prevent the accumulation of contaminants in the system. These include small dust and fiber particles, which can cause blockage of the liquid distribution section. To achieve a homogeneous liquid distribution across the 50 mm wide (W) falling film test section, the liquid is guided through a distributor slit with a height of 0.4 mm and length of 90 mm. To ensure the presence of a fully developed channel flow at the distributor outlet, the latter was chosen to be significantly larger than the maximum expected hydrodynamic entrance length ($L_{ch} < 20$ mm at $Re_{ch} < 1000$).[56] The optically accessible test section has a length of $L = 110$ mm, which allows for the investigation of structure effects isolated from the film's natural waviness developing at larger flow distances. Exemplarily, a wave-free entrance length of approximately 240 mm can be calculated for film flow on a smooth plate at a Reynolds number of $Re = 200$ and plate inclination angle of $\alpha = 60°$ based on a corrected version of a literature

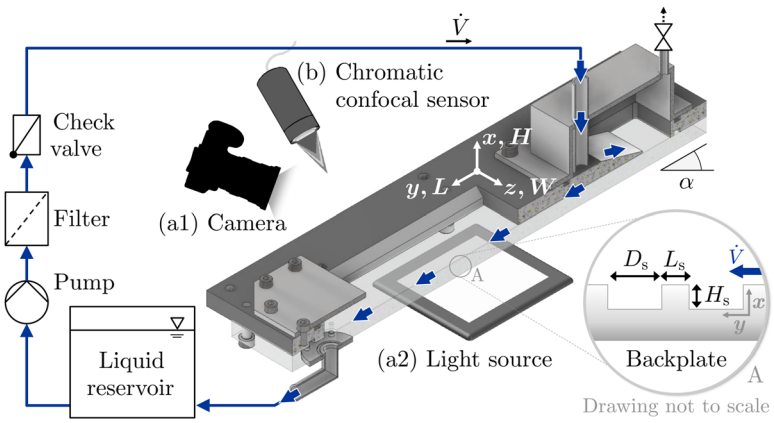

FIG. 1. Falling film test rig and schematic depiction of the investigated surface structure shape. The coordinate system origin is positioned on the plate surface, centrally across the plate width at the outlet of the liquid distributor.

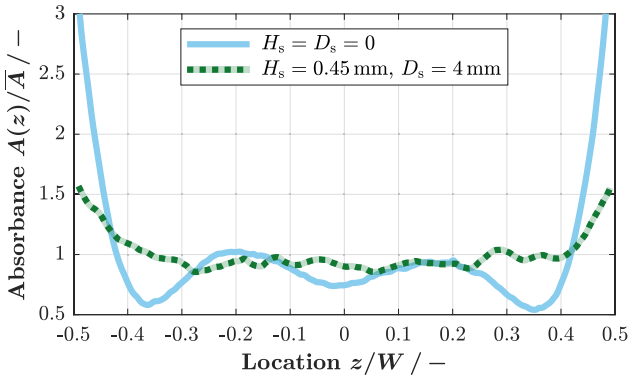

FIG. 2. Normalized absorbance recorded across the plate width W for a smooth and structured plate at $\alpha = 20.5°$ and $Re = 482$.

correlation[57,58] (see the supplementary material Sec. S1). The falling film apparatus and connected peripheral devices for data acquisition can be inclined at angles in the range of $\alpha = 0°$–$90°$, where 0° corresponds to a horizontal orientation.

A digital camera (D5300, Nikon) and LED-backlight (LLUB, PHLOX Corporation) are used for qualitative flow visualization. Furthermore, a chromatic confocal point sensor (CHRocodile 2S, Precitec) with a measurement range of 0–6 mm and a maximum measurement angle of ±30° is employed to quantitatively capture the wave dynamics.[59] It is important to note, that experimental results based on such point-wise measurement techniques can be influenced by sidewall effects. In the present study, this is observed especially for falling film flow on the smooth reference plate, where the rise of liquid at the sidewalls can lead to the formation of localized ridges and depressions even at greater wall distances. The employed point sensor is nevertheless considered suitable for use in the present study, as the investigated surface structures lead to a significant reduction of the wall-induced inhomogeneities. This effect is particularly pronounced for higher structure heights ($H_s \geq 0.32\,\text{mm}$), which is exemplarily visualized in Fig. 2. The figure shows the normalized absorbance of the liquid film dyed with methylene blue (see Sec. II B), which is a measure for changes in the local film thickness.[60] The data are extracted from color images of the falling film along a line across the plate width, at a distance of $y \approx 100\,\text{mm}$ downstream from the liquid distributor. For clarity, a Gaussian smoothing with a window size of about 0.9 mm is applied, and the curves are averaged over a series of 15 consecutive images. The point sensor is positioned in the center of the plate ($z/W = 0$), where the influence of the sidewalls on the observed film thickness is small for the structured plates considered here.

The experiments are conducted in an air-conditioned environment at ambient temperature ($\overline{T} = 21\,°\text{C}$). The corresponding liquid density, kinematic viscosity, and surface tension of $\rho = 997.99\,\text{kg/m}^3$, $\nu = 0.9798 \times 10^{-6}\,\text{m}^2/\text{s}$, and $\sigma = 72.59 \times 10^{-3}\,\text{N/m}$ are used to calculate characteristic film properties.[61]

B. Materials

Interchangeable back panels with varying rectangular surface corrugations oriented perpendicular to the falling film's main flow direction are machined from 10 mm thick acrylic glass sheets (Plexiglas XT, Röhm). As shown in Fig. 3, the distance and height of the investigated structure elements are systematically varied in the range of $D_s = 2$–$8\,\text{mm}$ and $H_s = 0.22$–$1.2\,\text{mm}$, respectively. The former is in the same order of magnitude as the capillary length $l_{Ca} = \sqrt{\sigma/(\rho g)} \approx 2.7\,\text{mm}$.[55] With respect to the Nusselt film thickness h_{Nu}, the latter is in the order of $0.3\,h_{Nu} < H_s < 3\,h_{Nu}$ under the experimental conditions considered here (see Sec. II C), thus falling within the range of structure heights proposed as promising for mass transfer applications in the literature.[42,45] The ridge length is maintained at $L_s = 0.7\,\text{mm}$ for all plates, unless otherwise specified. The accuracy of the manufacturing process is in the order of $\pm 20\,\mu\text{m}$.

De-ionized water is used as the working fluid and a small amount of methylene blue (CAS: 61-73-4) is added to the liquid phase at a concentration of 100 mg/kg (313 μM) to enhance the light contrast in the recorded images. Comparative surface tension measurements between pure and dyed de-ionized water in a bubble pressure tensiometer (BP100, Krüss) showed no significant influence of the dye on the surface tension [$\overline{\sigma}(25°\text{C}) = 70.92 \times 10^{-3}$ and $70.96 \times 10^{-3}\,\text{N/m}$ for pure water and the dyed aqueous solution used in this study, respectively]. Similarly, due to the low dye concentration, the influence of the solute on other physical properties such as ρ or ν is assumed to be negligible.

C. Experimental procedure and operating conditions

The chromatic confocal point sensor is centered along the width of the plate and placed at a distance of $y \approx 100\,\text{mm}$ downstream of the liquid distributor outlet. For each of the structured plates, the lengthwise sensor position is slightly adjusted so that the measurement spot is centered between two subsequent structure elements. Experiments are conducted at plate inclination angles of $\alpha = 20.5°$ and $\alpha = 60.6°$ to the horizontal. For each plate and inclination angle, the falling film flow is

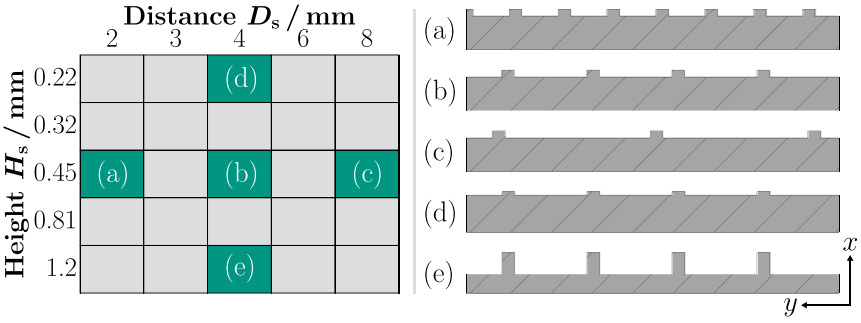

FIG. 3. Matrix representation of the surface structure modification (left) and exemplary visualization of selected structure geometries (right). The labels (a)–(e) refer to the positions in the matrix representation.

analyzed at six distinct Reynolds numbers in the range of $Re = 232–482$ with $\Delta Re = 50$. These values are higher than the critical Reynolds number for the onset of film rupture on the smooth reference plate under dewetting conditions and lower than the Reynolds number limit for the transition from laminar wavy to fully turbulent falling film flow. The former was determined to occur below $Re \approx 200$ in preliminary experiments, and the latter was calculated[62] to occur at $Re > 840$. In the investigated value range, the employed surface structures induce unsteady oscillatory surface deformations in the falling film. Such unsteady flows are characterized by higher heat and mass transfer rates than steady ones.[38,39,55] The Reynolds number is defined as[57]

$$Re = \frac{hu}{\nu} = \frac{q}{\nu}, \tag{1}$$

with the continuity condition $q = hu$, where h and u denote the local film thickness and thickness-averaged liquid velocity, respectively. It is calculated from the specific liquid load $q = \dot{V}/W$ or $\Gamma = \dot{m}/W$, which represents the volume flow rate $\dot{V}$ or mass flow rate $\dot{m}$ per unit width W of the plate. The investigated experimental parameter range is summarized in Table I. For the specified experimental conditions, the Nusselt film thickness is in the range of $h_{Nu} = 428–739\ \mu$m. The corresponding Nusselt correlation[63] was reported to be well applicable even beyond laminar flow conditions up to $Re \approx 400$,[62] and the deviations from correlations developed for laminar wavy or turbulent falling film flow[62,64] are below 10% within the investigated Re and α range. Nevertheless, the reported values are intended as a purely qualitative reference for the investigated structure heights H_s.

An experimental run consists of three phases, in each of which film thickness measurements are taken at all previously indicated Reynolds numbers Re while progressively reducing (phases 1 and 3) or increasing (phase 2) the liquid load. As the underlying measurement procedure relies on distance rather than direct film thickness measurements, reference measurements of the fully dried plate are taken at the beginning and end of each experimental run. Three consecutive experimental runs are carried out for every plate with the sensor being removed and reattached after each repetition to check for systematic errors. The falling film apparatus itself is not disassembled and reassembled between subsequent repetitions, as preliminary experiments with a reduced number of plates showed that systematic errors due to the reassembling are negligible compared to other error sources.

In all experiments, the sampling duration and frequency are set to $t \geq 20$ s and $f = 1200$ Hz, respectively. These values were chosen on the basis of preliminary test measurements (see the supplementary material Sec. S2). On the one hand, the sampling duration t is set sufficiently high to reduce the statistical error of key flow characteristics, such as the mean film thickness $\overline{h}$ or film thickness standard deviation s_h. On the other hand, the selected measurement frequency f is high enough to resolve individual waves in time. In addition to the quantitative sensor measurements, a series of images is captured at each Reynolds number Re setpoint in a fourth experimental run. These images are, however, not quantitatively processed and are merely intended for the qualitative assessment of the homogeneity of the liquid distribution across the plate.

TABLE I. Experimental parameter range.

Property	Unit	Value
H_s	mm	0.22, 0.32, 0.45, 0.81, 1.2
D_s	mm	2, 3, 4, 6, 8
L_s	mm	0.7
α	deg	20.5, 60.6
Γ	$g\,m^{-1}\,s^{-1}$	227, 276, 324, 373, 422, 471
Re	⋯	232, 282, 332, 382, 432, 482

D. Data evaluation

The transient sensor output signal $S(t)$ consists of a measured distance $d(t)$ as an indicator for the position of the gas–liquid interface and the signal intensity $I(t)$. To avoid the processing of erroneous signals due to daily varying scatter light from the environment, data points with signal intensities close to the mean scatter light intensity $\overline{I}_{sct}$ are discarded. The latter is measured after every start-up of the sensor. A subsequent outlier removal based on the interquartile range (IQR), which represents the difference between the third quartile (Q_3) and first quartile (Q_1) of the dataset, is applied. This yields the filtered time series $S^*(t)$ as formulated in Eq. (2), where $s_{I_{sct}}$ is the standard deviation of the scatter light intensity. It should be noted that the effect of the IQR filter was negligible in the vast majority of cases and was only necessary to correct irregular behavior of the intensity filter in a few limited instances (see the supplementary material Sec. S3),

$$S^*(t) = \left\{ S(t) \middle| I(t) \geq \overline{I}_{sct} + 2\,s_{I_{sct}}, d(t) \in [\,Q_1 - 3\mathrm{IQR}, Q_3 + 3\mathrm{IQR}] \right\}. \tag{2}$$

The film thickness time series $h(t)$ is calculated according to Eq. (3) with the mean distance between the sensor head and the dry backplate serving as reference value $\overline{d}_0$,

$$h(t) = \overline{d}_0 - d(t) \forall d(t) \in S^*(t). \tag{3}$$

The film thickness distribution's mean value $\overline{h}$ and standard deviation s_h serve as the key statistical characteristics. Additionally, wave-related parameters such as the median wave height $\tilde{h}_w$ as well as the median wave period $\tilde{t}_w$ and wave frequency $\tilde{f}_w$ are extracted by means of a zero-crossing analysis, as proposed for the investigation of wave dynamics in stratified[65] or annular[66] pipe flow. As proposed by Ayati and Carneiro,[65] the mean film thickness $\overline{h}$ is used as the reference value, which is subtracted from the time-dependent data $h(t)$. An individual wave cycle is then considered as the interval between two successive zero-down-crossings. The latter are defined as locations, at which five consecutive data points with positive sign are succeeded by five consecutive data points with negative sign. Before conducting the zero-crossing analysis, the film thickness time series is linearly interpolated ($\Delta t = 8.33 \times 10^{-5}$ s). The main parameters extracted from the analysis are schematically depicted in Fig. 4, where the mean film thickness $\overline{h}$ is also indicated (solid, horizontal line).

E. Order-of-magnitude estimates in the context of mass transfer applications

To derive first conclusions for mass transfer applications from the hydrodynamic analysis, this study relies on estimates of the factors,

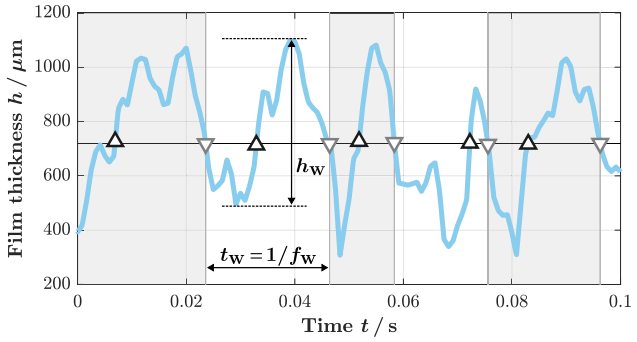

FIG. 4. Zero-crossing analysis on an exemplary film thickness time series (H_s = 0.45 mm, D_s = 6 mm, α = 60.6°, and Re = 382) with individual wave cycles indicated by alternating shading and zero-up-crossings (zero-down-crossings) marked by △ (▽).

by which the surface structuring could contribute to increase the gas–liquid interfacial area S ($F_S = S_{\text{struct.}}/S_{\text{smooth}}$) or liquid residence time τ ($F_\tau = \tau_{\text{struct.}}/\tau_{\text{smooth}}$). To determine F_S, the film thickness time series $h(t)$ is converted into a spatial wave through multiplication with the mean film velocity $\overline{u}$. The latter is approximated from the mean film thickness $\overline{h}$ using the continuity condition in Eq. (1) ($\overline{u} \sim 1/\overline{h}$) and assuming a homogeneous flow distribution across the entire film thickness. The lengths of the connecting lines between successive data points are then summed and the resulting interfacial length is referenced to its 1 D projection length. It should be noted, that the assumption of homogeneous flow distribution may lead to an underestimation of the actual flow velocity, particularly in the case of increased structure heights and low structure distances, where the moving fluid may not reach the bottom of the trenches between the individual structure elements. Moreover, the estimation procedure does not capture the increase in the gas–liquid interfacial area due to the three-dimensional nature of the evolving waves.

The factor, by which the surface structuring increases the mean film thickness is used as a rough indicator for changes in liquid residence time ($F_\tau \sim \overline{u}_{\text{smooth}}/\overline{u}_{\text{struct.}} \sim \overline{h}_{\text{struct.}}/\overline{h}_{\text{smooth}}$). In addition to the previously described limitations, this does not consider the effects of internal recirculation zones or superimposed transversal fluid motion on the liquid residence time. Overall, the determined factors should be considered as mere order-of-magnitude estimates.

III. RESULTS AND DISCUSSION

Section III A presents a qualitative classification of the falling film flow patterns observed in this study. Subsequently, the influence of structure geometry, Reynolds number, and plate inclination angle on the wave dynamics is analyzed quantitatively in Sec. III B, with a particular focus on the evolution of strongly oscillating flow patterns. Finally, the potential implications of the findings from the hydrodynamic analysis for mass transfer applications are discussed in Sec. III C.

A. Qualitative film flow classification

Due to the use of a localized measurement technique, only falling film flows with a homogeneous liquid distribution can be statistically evaluated. To identify experimental setpoints resulting in unstable or maldistributed flows and exclude them from the quantitative analysis, a qualitative film flow classification is introduced, as depicted in Fig. 5. From a more practical standpoint, the derived flow pattern maps are useful for determining the operational limits, within which a particular structure geometry could be employed in a technical application. Based on the recorded camera images, film flow is classified as belonging to the first applicable flow pattern in the order indicated in the figure. While the exact conditions, under which a particular category applies, may be affected by manufacture-dependent substrate properties, such as the structure element's edge sharpness, it is expected that the mere existence of the observed flow patterns and general trends for the transition between them can be generalized.

The influence of the structure geometry and liquid flow rate on the film flow classification for liquid flow over structured surfaces inclined at $\alpha = 20.5°$ to the horizontal is depicted in Fig. 6 (top). Even at the lowest investigated Reynolds number ($Re = 232$), homogeneous flow distribution (flow pattern D) is reached for structure configurations with either low structure heights ($H_s = 0.22$ mm) or distances ($D_s = 2$ mm), the latter possibly due to flow stabilization by an unmoving liquid sublayer forming between the structure elements. In contrast, a combination of medium structure heights 0.32 mm $\leq H_s \leq$ 0.81 mm and medium to large structure distances 3 mm $\leq H_s \leq$ 8 mm can cause random temporary dewetting primarily on top of the sharp-edged structure elements (flow pattern C) or lead to permanent liquid maldistribution (flow pattern B). The latter represents an unfavorable flow condition for, e.g., falling film heat

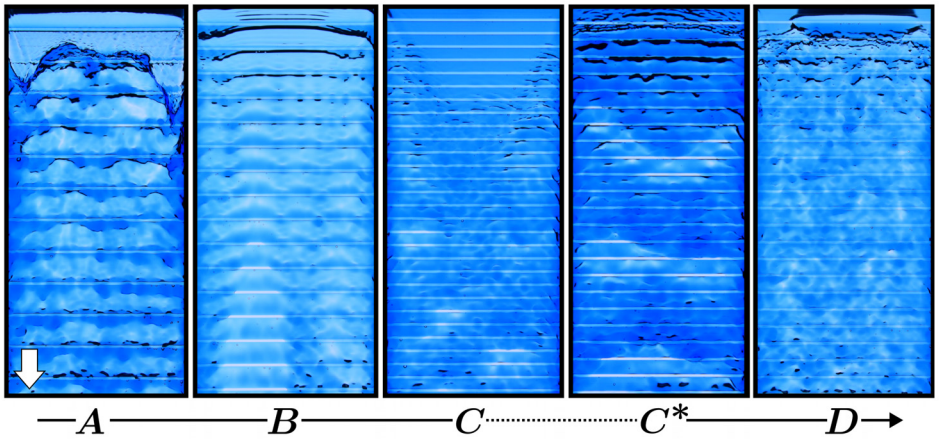

FIG. 5. Film flow classification: film detachment (A), permanent liquid maldistribution (B), temporary dewetting at random locations (C) or across the full plate width (C*), and homogeneous falling film (D). The flow direction is indicated by a white arrow.

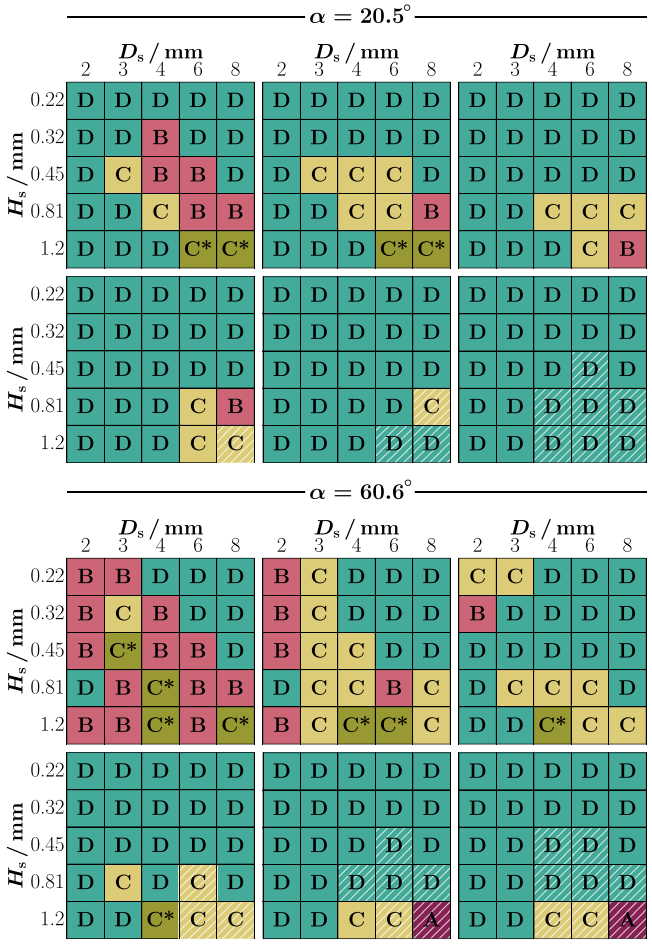

FIG. 6. Influence of structure geometry and Reynolds number (from top left to bottom right: $Re = 232, 282, 332, 382, 432, 482$) on the film flow classification at $\alpha = 20.5°$ (top) and $\alpha = 60.6°$ (bottom). Gas bubble formation is indicated by hatching.

exchangers or absorbers, as it may result in a significant reduction of local heat and mass transfer rates.[67] Moreover, at low Reynolds numbers, structure elements with $H_s = 1.2$ mm and $D_s \geq 6$ mm can represent individual obstacles to the liquid flow instead of collectively affecting the flow evolution. The associated temporary accumulation of liquid upstream of the structure elements results in the formation of high-wavelength, high-amplitude waves (flow pattern C*). Such traveling "disturbance waves"[66] can cause uniform, temporary dewetting across the entire plate width.

With increasing Reynolds number, liquid maldistribution and temporary dewetting occur less frequently. At the same time, gas bubble formation in the upper part of the structured plate and subsequent bubble entrainment with the liquid flow is observed at $Re \geq 382$ (see the supplementary material Sec. S4). Such bubble formation can occur in the presence of breaking waves[68] or hydraulic jumps.[69] With respect to heat and mass transfer applications, this phenomenon would undoubtedly result in an increase in the effective gas–liquid interfacial area and disturbance of the liquid layers close to the bottom of the trenches. However, depending on the design of the liquid outlet, it can also lead to the unfavorable removal of gas phase species along with the liquid phase.

Increased plate inclination angles generally lead to film thinning and reduced film stability.[70] As can be taken from Fig. 6 (bottom), this results in stronger maldistribution and dewetting effects as well as increased bubble entrainment at higher inclination angles but identical Reynolds numbers. Moreover, at high flow rates ($Re \geq 432$), the flow disturbance induced by structure elements with $H_s = 1.2$ mm and $D_s = 8$ mm can become so drastic that the liquid film permanently detaches from the wall in the upstream section of the structured plate (flow pattern A). This "teapot effect"[71] is strongly dependent on the experimental configuration (see the supplementary material Sec. S5). More specifically, a higher distance between the liquid distributor outlet and the structured plate section as well as an increased distributor height can help to significantly delay the film detachment. The same applies to structure elements with increased length L_s in a streamwise direction. Despite its dependence on the experimental configuration, the observed film detachment exemplifies that the use of certain structure geometries may be accompanied by a reduction of the applicable Reynolds number operating window. In small system configurations, this could be counteracted by the implementation of active control strategies, e.g., the flexible adaption of the plate inclination angle α depending on the liquid load. Such a concept was proposed by Reitze *et al.*[72] for the production of specialty chemicals in a wetted wall distillation column.

From a methodological point of view, regarding the statistical evaluation of the local sensor measurements in Sec. III B, liquid detachment or maldistribution close to the measurement point can lead to a distortion of the determined film characteristics. The data recorded at $Re = 232$ and $Re = 282$ are, therefore, excluded from the quantitative analysis. In contrast, temporary dewetting is not expected to have an unfavorable effect on the measurement results and the employed chromatic confocal point sensor is assumed to be suitable for capturing the overall film statistics under these conditions. However, a comprehensive assessment of the full three-dimensional nature of the evolving waves (see, e.g., Fig. 5, right) is not possible with the employed pointwise measurement method and is beyond the scope of this study.

B. Wave dynamics

This section presents a quantitative analysis of the wave dynamics associated with falling film flows on structured surfaces. Initially, structure geometries that induce particularly strong interfacial oscillations are identified. These may be of particular interest for mass transfer applications. Subsequently, the influence of Reynolds number and plate inclination on the observed flow phenomena is discussed.

1. Influence of structure geometry

The transient interface deformation is significantly influenced by changes in the structure geometry of the falling film wall. This is discussed in detail below for a constant inclination angle of $\alpha = 20.5°$ and a constant Reynolds number of $Re = 482$. Exemplary film thickness time traces, determined with the chromatic confocal point sensor, are depicted in Fig. 7 for the smooth reference plate as well as for structured surfaces with a structure height of $H_s = 0.45$ mm and varying structure distances of $D_s = 2$–8 mm. These time traces represent the

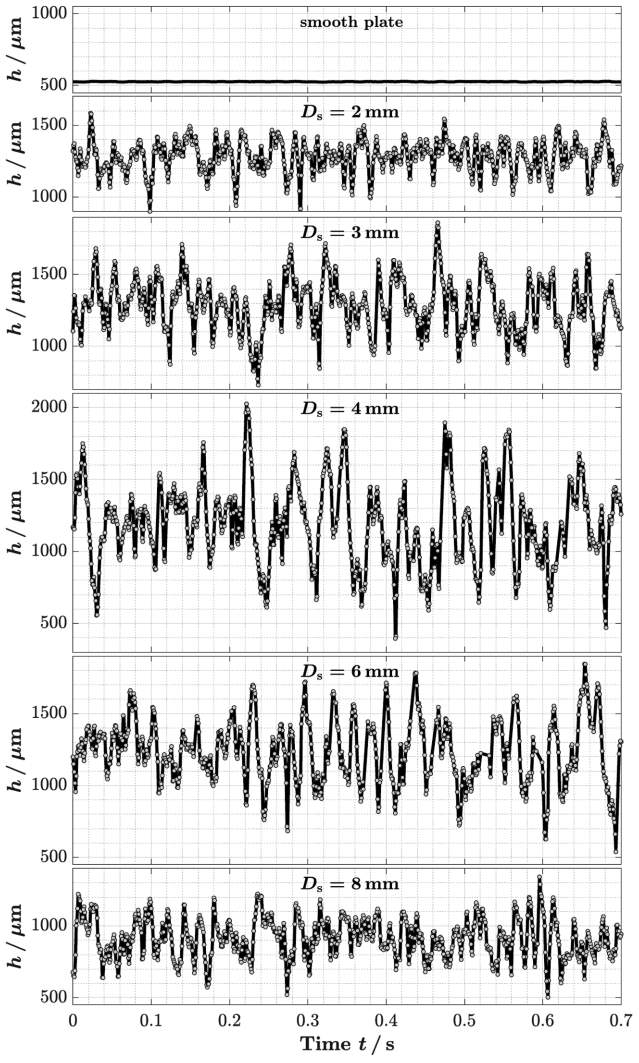

FIG. 7. Film thickness time traces determined at $\alpha = 20.5^\circ$ and $Re = 482$ for the smooth reference plate as well as for structured surfaces with $H_s = 0.45$ mm and $D_s = 2$–8 mm. Linear interpolations (solid line) are shown in addition to the measured data points (circles).

starting point for the subsequent statistical evaluation and zero-crossing analysis.

The influence of the structure distance D_s on the film thickness distribution is summarized in Fig. 8 for $H_s = 0.45$ mm. The figure displays the film thickness time series, partially shown in Fig. 7, in the form of histograms. Normal distributions fitted to the respective raw data are indicated by solid lines. Irrespective of the structure distance D_s, falling film flow over structured surfaces with $H_s = 0.45$ mm is characterized by much broader film thickness distributions than falling film flow over the smooth reference plate under otherwise identical conditions. These broader distributions indicate significantly more pronounced transient wave instabilities in the film flow over the structured surfaces. The exact film dynamics are strongly influenced by the structure distance D_s. First, a shift toward lower average film

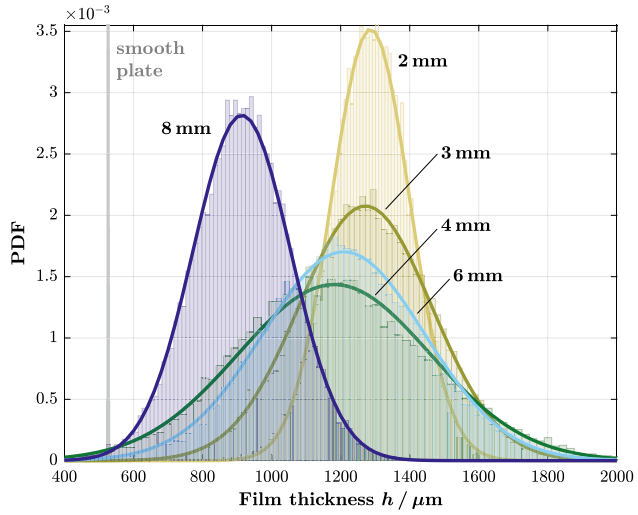

FIG. 8. Influence of the structure distance D_s on the film thickness distribution for film flow over structured surfaces with $H_s = 0.45$ mm in comparison to the smooth reference plate at $\alpha = 20.5^\circ$ and $Re = 482$.

thicknesses $\overline{h}$ can be noted with increasing structure distance, i.e., from $D_s = 2$ mm to $D_s = 8$ mm, which is due to the increased distance between the measurement point and the surface elevation in the vicinity of the structure elements. This effect is visualized in Fig. 9(a), where the mean surface elevation $\overline{x} = f(\overline{h}, H_s)$, representing the distance between the gas–liquid interface and the plate surface, is plotted for the five different measurement point positions shown in Fig. 9(c). Second, the film thickness distributions initially broaden from $D_s = 2$ mm to $D_s = 4$ mm, as the film flow can penetrate more deeply into the grooves between the structure elements and the main flow direction is disturbed more strongly. Beyond this point, i.e., for $D_s \geq 6$ mm, a reverse trend is observed and the distributions narrow, indicating a reduction in the oscillatory wave height h_w with a further increase in structure distance. This can be attributed to the reduced interaction between flow distortions induced at subsequent ridges. As illustrated in Fig. 9(b), the observed behavior is not exclusive to the chosen default measurement position [index (3) in Fig. 9(c)], but can be observed regardless of the exact location of the measurement point, despite variations in absolute values.

Overall, an "optimum" structure distance around $D_s^* \approx 4$ mm is identified from Fig. 8, at which the film thickness distribution reaches a maximum spread due to strong surface oscillations being induced in the falling film. Structure distances much lower ($D_s = 2$ mm) or higher ($D_s = 8$ mm) than the optimum value excite the falling film flow to a much lesser extent, either because the liquid is skimming over the less elevated plate sections between the structure elements or because single, non-interacting surface distortions are induced close to the ridges.[35,49] A similar "resonance" phenomenon was observed for the static deformation of falling film flows over surfaces with sinusoidal[49,50,52,73] or rectangular[53,54,74] corrugations. For linear resonance, the surface amplification was reported to be strongest when the wavelength of the structured surface is in the order of $\lambda_s = D_s + L_s \approx 2\pi h_{Nu}$.[52,73] The thereby estimated optimum structure wavelength for maximum static surface amplification $\lambda_s^* \approx 5$ mm ($\alpha = 20.5^\circ$,

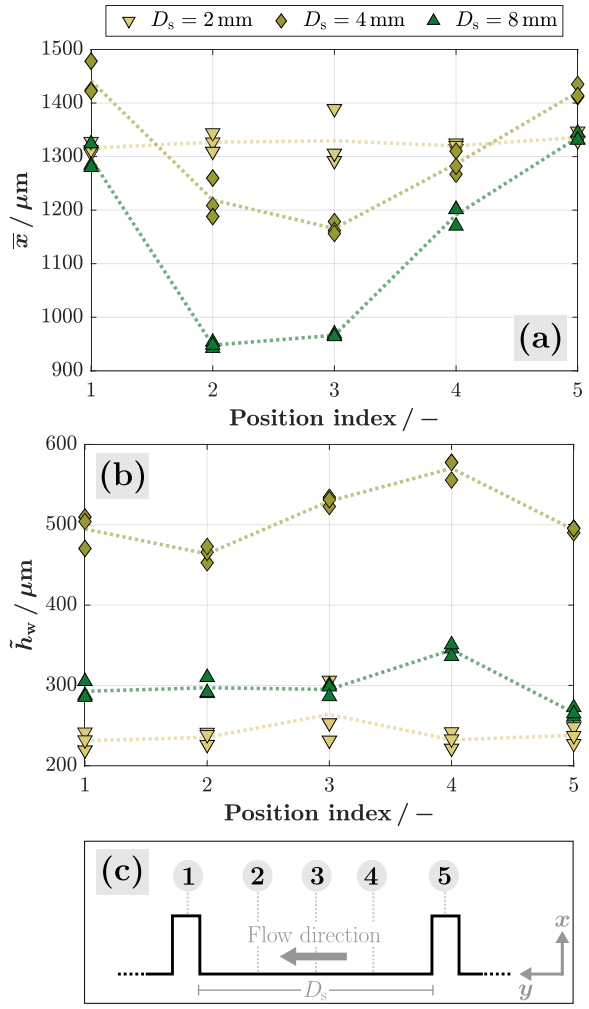

FIG. 9. Mean surface elevation $\bar{x}$ (a) and median wave height $\tilde{h}_w$ (b) determined at five different measurement points (c) for structured plates with $H_s = 0.45\,\mathrm{mm}$ and $D_s = 2,\ 4,$ and $8\,\mathrm{mm}$ ($Re = 482$ and $\alpha = 20.5°$). Three measurement repetitions are shown.

$Re = 482$) is in the same value range as the structure wavelength, at which the most pronounced dynamic surface oscillation is observed in the present study. Consequently, the strong transient instabilities observed for $D_s = 4\,\mathrm{mm}$ ($\lambda_s = 4.7\,\mathrm{mm}$) may result from the interaction of traveling disturbances and inertia-induced flow features with a statically deformed base flow under resonance-like conditions. While dynamic surface oscillations were observed previously, they were reported to be much smaller than the static surface deformation.[53] The rather pronounced transient destabilization observed here may be attributed to the relatively narrow ridge lengths L_s in the streamwise direction, as discussed in greater detail in Sec. III B 2. It should be noted that Davies and Warner[35] associate a similar oscillatory film flow behavior with the interference of internal vortices forming in the vicinity of successive structure elements, rather than with a resonance interaction. However, no hydrodynamic analyses were provided to support this hypothesis, and numerical simulations by Åkesjö *et al.*[38] indicate the occurrence of highly time-dependent and locally isolated recirculation zones for film flow over a surface with wire-shaped structure elements.

The same structure-induced flow destabilization can be observed for different structure heights H_s. This is discussed below on the basis of characteristic wave properties, namely, the median wave height $\tilde{h}_w$ and wave frequency $\tilde{f}_w$, which were determined by a zero-crossing analysis. Complementary data from a purely statistical analysis is provided in the supplementary material Sec. S6, where the wave dynamics results for the other operating conditions investigated are also given. The median wave height $\tilde{h}_w$ is plotted in Fig. 10(a) as a function of the structure distance-to-height ratio D_s/H_s for falling film flow at $Re = 482$ and $\alpha = 20.5°$. The corresponding mean film thickness $\bar{h}$ is shown in Fig. 10(b) for the structured surfaces and smooth reference plate. In the case of the latter, a height correction derived from widthwise changes in local light absorbance (see Fig. 2) is applied to minimize distortions due to sidewall effects. In the graphs, each symbol represents a single measurement, that was repeated nine times for each condition. This illustrates the generally high reproducibility of the measurements.

As can be taken from Fig. 10(a), the maximum transient free-surface deformation identifiable at a specific structure distance D_s for each of the investigated structure heights H_s is amplified with increasing structure height. The corresponding peak median wave heights $\tilde{h}_w^*$ are in the order of the structure height. The absolute values range from $\tilde{h}_w^* = 251\,\mu\mathrm{m}$ at $H_s = 0.22\,\mathrm{mm}$ to $\tilde{h}_w^* = 923\,\mu\mathrm{m}$ at $H_s = 1.2\,\mathrm{mm}$, corresponding to 23% and 48% of the mean film thickness $\bar{h}$, respectively. This growth of the structure-induced interfacial oscillations with increasing structure height is accompanied by a slight shift of the structure distance D_s, at which the peak waviness is reached, toward higher values. More specifically, the optimum distance increases from $D_s^* \approx 3\,\mathrm{mm}$ at $H_s = 0.22\,\mathrm{mm}$ to $D_s^* \approx 4\,\mathrm{mm}$ at $0.32\,\mathrm{mm} \le H_s \le 0.45\,\mathrm{mm}$ and $D_s^* \approx 6\,\mathrm{mm}$ at $0.81\,\mathrm{mm} \le H_s \le 1.2\,\mathrm{mm}$. Following the line of reasoning for steady falling film flow over a single step-out,[5] this may be due to the elongation of the flow path in the vicinity of the structure elements, along which momentum is transformed from streamwise to cross-stream direction. Consequently, inertia-induced surface deformations become more pronounced with increasing structure height, which enables the interaction of flow features induced by structure elements located at greater distances. As can be estimated from the analysis by Bontozoglou and Serifi[5] for steady film flow over a single step, such inertial features dominate the liquid behavior over capillary features under the majority of the flow conditions investigated in this study. Especially at high Reynolds numbers Re, structure distances D_s, and structure heights H_s, their occurrence is expected to induce additional transient instabilities in the film flow. The effect is magnified by the relatively low ridge lengths considered in this study (see Sec. III B 2). Whether the corresponding streamwise lengthscale of the inertial ridge[5] could be a useful parameter in determining the optimum structure distance D_s^* from a theoretical perspective, remains an open question beyond the scope of this study.

As shown in Fig. 10(c), an inverse trend can be observed for the median wave frequency $\tilde{f}_w$ in comparison to the median wave height. A maximum in the wave height curve $\tilde{h}_w = f(D_s/H_s)$ is usually accompanied by a minimum in the wave frequency curve $\tilde{f}_w = f(D_s/H_s)$, which may indicate the existence of a limiting wave steepness. Absolute values range from $\tilde{f}_w^* = 19\,\mathrm{Hz}$ at $H_s = 1.2\,\mathrm{mm}$ to

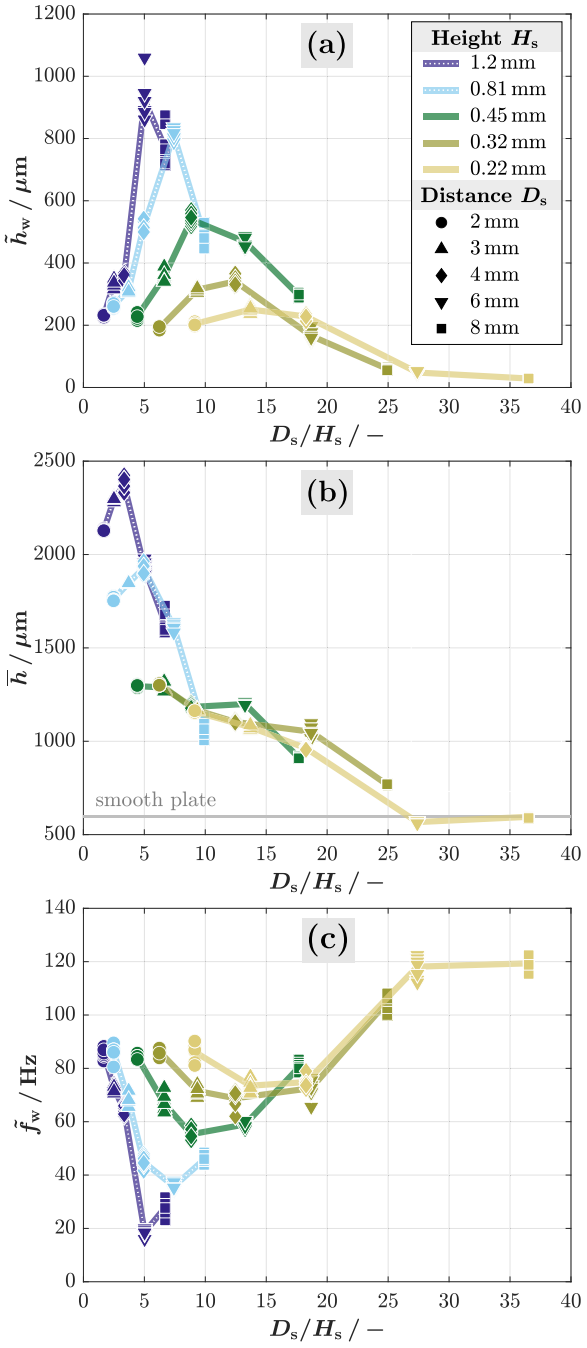

FIG. 10. Median wave height $\tilde{h}_w$ (a), mean film thickness $\bar{h}$ (b), and median wave frequency $\tilde{f}_w$ (c) as a function of the structure distance-to-height ratio D_s/H_s at $\alpha = 20.5°$ and $Re = 482$. The mean film thickness determined for the smooth reference plate is indicated in (b) by a solid line. Nine repetitions are shown for each data point.

$\tilde{f}_w^* = 74$ Hz at $H_s = 0.22$ mm. With regard to the wave dynamics, this illustrates that irrespective of the structure height H_s, an increase in the structure distance D_s initially results in the transformation of small surface ripples prevalent at low D_s into high-amplitude, low-frequency surface deformations observable at higher D_s. However, this effect is reversed after a certain optimum structure distance D_s^* is exceeded. Qualitatively, this can already be observed visually in the film thickness time traces shown in Fig. 7.

2. Influence of Reynolds number and inclination angle

Section III C 2 is dedicated to analyzing how robust the previously described falling film flow behavior and determined optimum geometric parameters are to changes in Reynolds number Re and inclination angle α. This is discussed below using the median wave height $\tilde{h}_w$ as a key parameter to characterize the oscillatory film dynamics. From a practical point of view, such an analysis helps to assess, whether the same surface structures could be suitable under varying flow conditions or in different system configurations.

The influence of Reynolds number Re and structure height H_s on the median wave height $\tilde{h}_w$ is displayed in Figs. 11(a) and 11(b) for inclination angles of $\alpha = 20.5°$ and $\alpha = 60.6°$, respectively. Although the results are shown for a fixed structure distance of $D_s = 4$ mm, similar conclusions could be drawn for the other structure distances considered in this study. For low to medium structure heights $H_s \leq 0.45$ mm the median wave height $\tilde{h}_w$ increases proportionally with both Re and H_s. In contrast, nonlinear behavior is observed at higher structure heights $H_s \geq 0.81$ mm. This indicates the prevalence of more complex flow features, which can be strongly affected by varying inclination angle α. Such flow features include long-wavelength traveling waves, which can be induced in the falling film at low Re due to temporary liquid accumulation upstream of structure elements with high H_s (flow pattern C* in Fig. 5). The evolution of inertia-controlled flow features due to liquid overshoot perpendicular to the main flow direction plays another important role. With respect to the resulting free-surface deformation, potential saturation effects could contribute to the observed complex dependence on Re.

The aforementioned inertial effects have a particularly destabilizing influence on the film flow in the case of the default low ridge length of $L_s = 0.7$ mm in the streamwise direction. This is illustrated in Fig. 12, where the median wave height $\tilde{h}_w$ is plotted as a function of Reynolds number Re for structured surfaces with constant structure height $H_s = 1.2$ mm and structure distance $D_s = 8$ mm but varying ridge length L_s. On the one hand, significantly higher median wave heights $\tilde{h}_w$ are generally observed for $L_s = 0.7$ mm than for $L_s = 2$ mm or $L_s = 4$ mm. On the other hand, for reduced ridge lengths, the change in $\tilde{h}_w$ with Reynolds number Re deviates from the proportional behavior observed at the highest considered ridge length ($L_s = 4$ mm). The destabilizing effect of narrow ridges on the film flow is qualitatively visualized in Fig. 13. While pronounced liquid overshoot is observed for $L_s = 0.7$ mm [marker (D) in Fig. 13(a)], this flow feature is much less prevalent for the other two investigated L_s.

As described above, the absolute values of the median wave heights $\tilde{h}_w$ vary with both Reynolds number Re and inclination angle α. In contrast, the structure distances D_s or structure distance-to-height ratios D_s/H_s at which the maximum values $\tilde{h}_w^*$ are observed remain unaffected by changing Re and α, within the resolution limit of the discrete plate geometries investigated (see the supplementary material Sec. S6). From a practical point of view, this suggests that surface structures optimized for a particular Re and α setpoint may also be promising candidates for other flow conditions within the operating window investigated here ($Re = 332$–482 and $\alpha = 20.5°$–$60.6°$).

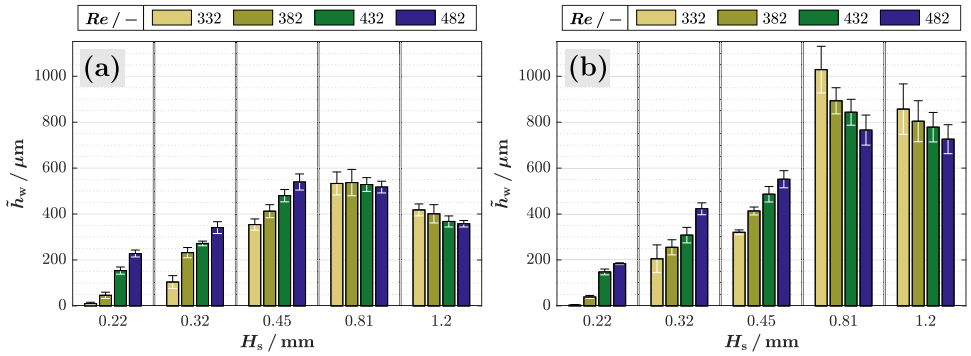

FIG. 11. Median wave height $\tilde{h}_w$ as a function of Reynolds number Re and structure height H_s for inclination angles of $\alpha = 20.5°$ (a) and $\alpha = 60.6°$ (b) ($D_s = 4$ mm). The error bars indicate plus/minus two times the standard deviation from nine measurement repetitions.

C. Potential implications for mass transfer applications

In the context of mass transfer applications, e.g., in falling film absorbers, the degree of utilization of the liquid phase can benefit from an increased gas–liquid interfacial area, higher liquid residence time in the apparatus, and intensified cross-stream convection within the liquid phase due to internal recirculation zones. As these factors are influenced by wave evolution, they are closely linked to the hydrodynamics of the falling film flow. Thus, after identifying structure geometries that excite particularly strong interfacial oscillations in Sec. III B, this section builds upon the hydrodynamic analysis to derive potential implications of the observed phenomena on mass transfer applications.

For this purpose, the factors by which surface structuring may contribute to increase the gas–liquid interfacial area (F_S) and liquid residence time (F_τ) are approximated from the experimental results, as described in Sec. II E. Again, it is important to emphasize, that the underlying point-wise measurement method does not capture the three-dimensional nature of the evolving waves or the actual internal flow conditions, e.g., local film velocities and internal mixing structures. Consequently, the presented results should be regarded as mere order-of-magnitude estimations. As illustrated in Fig. 14, the increase in the gas–liquid interfacial area due to surface structuring is in the order of 1%–10%. The peak values are reached for the structure geometries inducing interfacial oscillations with particularly high amplitudes (see Sec. III B 1). The absolute value range is considerably lower than the one obtained for the factor, by which surface structuring increases the mean film thickness and may thus contribute to increase the liquid residence time in comparison to the smooth reference plate [see raw data in Fig. 10(b)]. Exemplarily, for a structure height of $H_s = 0.45$ mm and structure distance of $D_s = 4$ mm, values of $F_S = 1.03$ and $F_\tau = 1.98$ are determined. Despite the inaccuracies associated with the estimation procedure, the vast discrepancy may suggest that, in the case of full plate wetting, the structure-induced increase in the gas–liquid interfacial area is of secondary importance compared to the increase in liquid residence time. In this context, the formation of internal recirculation zones can be expected to play another major role.

A review of the data presented by Davies and Warner[35] lends support to this hypothesis. The authors conducted mass transfer experiments on surface structures similar to the ones investigated here, albeit within a limited geometric parameter range. At $\alpha = 25°$ and

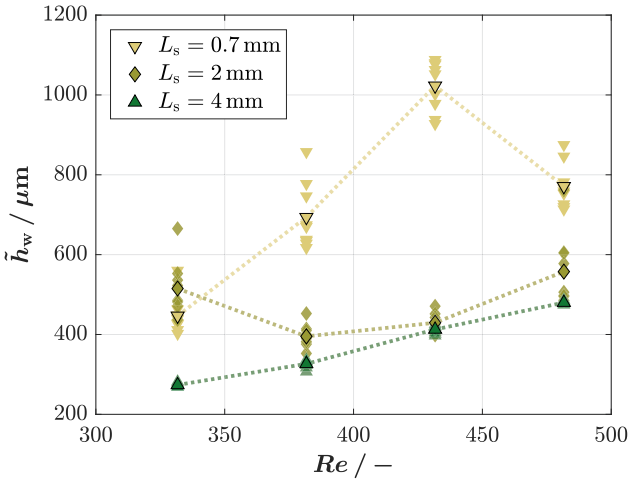

FIG. 12. Median wave height $\tilde{h}_w$ as a function of Reynolds number Re for different ridge lengths L_s ($H_s = 1.2$ mm, $D_s = 8$ mm, and $\alpha = 20.5°$). For every setpoint, the overall mean and nine individual measurement repetitions are indicated by markers with black and transparent outline, respectively.

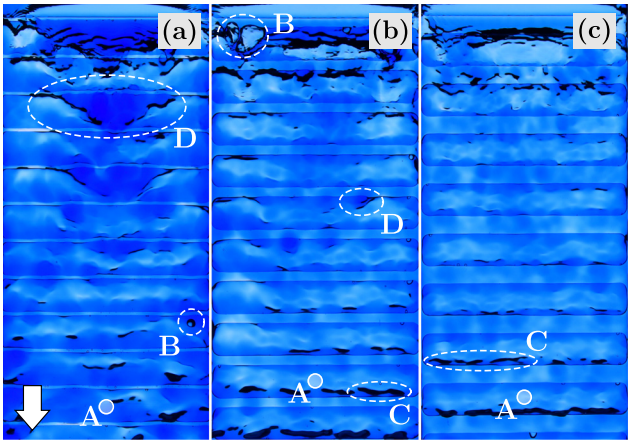

FIG. 13. Top view of film flow over structured surfaces with ridge lengths of $L_s = 0.7$ mm (a), $L_s = 2$ mm (b), and $L_s = 4$ mm (c). The position of the measurement point (A) and examples of bubble entrainment (B), steep interface curvature (C), and liquid overshoot (D) are highlighted ($H_s = 1.2$ mm, $D_s = 8$ mm,

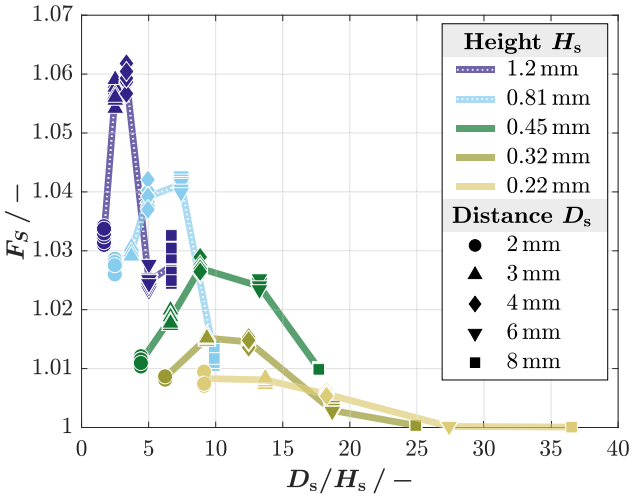

FIG. 14. Estimated increase in the gas–liquid interfacial area F_S as a function of the structure distance-to-height ratio D_s/H_s at $\alpha = 20.5°$ and $Re = 482$. Estimates from nine repeated datasets are shown.

$Re = 550$, they observed the most pronounced increase in the global mass transport coefficient at a structure distance-to-height ratio of $D_s/H_s = 5$ ($H_s = 1.3$ mm) for a constant structure distance of $D_s = 6.4$ mm. Similarly, an optimum was identified at $D_s/H_s = 4.7$ ($D_s = 9$ mm) for a constant structure height of $H_s = 1.9$ mm. In these cases, an increase in the mass transfer coefficient by a factor of 3.2 was reported, which is considerably larger than the maximum increase in the gas–liquid interfacial area estimated here for similar structure geometries and flow conditions. With respect to the geometric parameters, it can be observed that the optimum structure distance-to-height ratio determined by Davies and Warner[35] at $H_s = 1.3$ mm coincides with the value, at which the most pronounced free-surface deformation was determined in the present study for $H_s = 1.2$ mm. Moreover, comparing the two reported optimum values[35] supports the observed trend of increasing optimum structure distance D_s and decreasing optimum structure distance-to-depth ratio D_s/H_s with higher structure heights H_s from a mass transfer point of view. This comparison emphasizes the link between pronounced, unsteady free-surface deformation and intensified mass transfer in falling film flow configurations.

IV. CONCLUSION

This contribution features a systematic experimental investigation of the influence of surface structure modification on the wave dynamics of falling film flows. Particular emphasis is placed on identifying structure configurations that induce strong transient instabilities in the film flow, as unsteady flows are of particular interest for optimizing mass transfer applications,[55] such as falling film absorbers. The investigated surface structures consist of arrays of rectangular ridges oriented perpendicular to the main flow direction. The evolving flow patterns are analyzed qualitatively from image recordings and characterized quantitatively using a point-wise measurement technique. A full characterization of the three-dimensional nature of the evolving waves remains elusive with the employed measurement method and should be addressed in future works.

Within the investigated parameter range, an optimum structure distance exists, at which particularly strong interfacial oscillations are induced in the falling film. These could result from the interaction of the flow with a statically deformed base film under resonance-like conditions. The optimum structure distance increases with increasing structure height but is robust to changes in Reynolds number and plate inclination angle. The transient destabilization is amplified at narrow ridge lengths in the streamwise direction, where inertia-induced flow features due to liquid overshoot in the vicinity of the structure elements are particularly pronounced. This can lead to highly complex flow behavior, especially for increased structure heights. With regard to the optimization of mass transfer applications, the structure-induced increase in gas–liquid interfacial area may be of secondary importance compared to changes in internal flow conditions, namely, the increase in liquid residence time and intensified convective mixing. Future numerical investigations would be useful to visualize and quantify the formation of recirculation zones within the liquid phase for the determined optimum structure configurations. Literature results derived from the analysis of the global mass transfer characteristics of a falling film absorber[35] can be well integrated with the main findings from this hydrodynamic analysis. This highlights the relation between strong interfacial oscillations and enhanced mass transfer characteristics of falling film flows.

SUPPLEMENTARY MATERIAL

See the supplementary material for further information on data processing and calculation methods (Secs. S1–S3) as well as on qualitatively observed flow patterns (Secs. S4 and S5). Additional results on falling film wave dynamics (Sec. S6) are also provided.

ACKNOWLEDGMENTS

The authors extend their sincere thanks to Professor Olaf Deutschmann (Institute for Chemical Technology and Polymer Chemistry, KIT), Professor Hans-Jörg Bauer (Institute of Thermal Turbomachinery, KIT), and Dr. Rainer Koch (Institute of Thermal Turbomachinery, KIT) for fruitful scientific discussions and for providing laboratory infrastructure as well as experimental equipment. The authors also thank M.Sc. Fabio Öhl and B.Sc. Sinan Sarikaya for conducting preliminary tests related to the works presented in this contribution. Financial support by the Friedrich and Elisabeth Boysen Foundation (Project-ID Boy-165) and the Helmholtz program "Materials and Technologies for the Energy Transition, Germany" (MTET, 38.03.04) is gratefully acknowledged.

AUTHOR DECLARATIONS

Conflict of Interest

The authors have no conflicts to disclose.

Author Contributions

A. Düll: Data curation (lead); Formal analysis (lead); Investigation (lead); Methodology (lead); Software (lead); Validation (equal); Visualization (lead); Writing – original draft (lead); Writing – review & editing (supporting). **A. Cros-Le Lagadec:** Investigation (supporting). **J. Buchmüller:** Formal analysis (supporting); Investigation (supporting). **T. Häber:** Formal analysis (supporting); Funding acquisition (supporting); Methodology (supporting); Project administration

(lead); Supervision (lead); Validation (equal); Writing – review & editing (lead). **C. Ateş:** Conceptualization (equal); Funding acquisition (lead); Supervision (supporting); Writing – review & editing (supporting). **M. Börnhorst:** Conceptualization (equal); Funding acquisition (lead); Supervision (supporting); Writing – review & editing (supporting).

DATA AVAILABILITY

The data that support the findings of this study are available from the corresponding authors upon request.

REFERENCES

[1]R. V. Craster and O. K. Matar, "Dynamics and stability of thin liquid films," Rev. Mod. Phys. **81**, 1131–1198 (2009).
[2]L. Kahouadji, A. Batchvarov, I. T. Adebayo, Z. Jenkins, S. Shin, J. Chergui, D. Juric, and O. K. Matar, "A numerical investigation of three-dimensional falling liquid films," Environ. Fluid Mech. **22**, 367–382 (2022).
[3]S. Veremieiev, "Gravity-driven continuous thin film flow over topography," Ph.D. thesis (University of Leeds, 2011).
[4]A. Åkesjö, M. Gourdon, A. Jongsma, and S. Sasic, "Enhancing industrial vertical falling film evaporation through modification of heat transfer surfaces – An experimental study," Chem. Eng. Process. **191**, 109456 (2023).
[5]V. Bontozoglou and K. Serifi, "Falling film flow along steep two-dimensional topography: The effect of inertia," Int. J. Multiphase Flow **34**, 734–747 (2008).
[6]N. K. Lampropoulos, Y. Dimakopoulos, and J. Tsamopoulos, "Transient flow of gravity-driven viscous films over substrates with rectangular topographical features," Microfluid. Nanofluid. **20**, 51 (2016).
[7]S. Varchanis, Y. Dimakopoulos, and J. Tsamopoulos, "Steady film flow over a substrate with rectangular trenches forming air inclusions," Phys. Rev. Fluids **2**, 124001 (2017).
[8]D. Barreiro-Villaverde, A. Gosset, and M. A. Mendez, "On the dynamics of jet wiping: Numerical simulations and modal analysis," Phys. Fluids **33**, 062114 (2021).
[9]A. Gosset and J.-M. Buchlin, "Jet wiping in hot-dip galvanization," J. Fluids Eng. **129**, 466–475 (2006).
[10]M. Mendez and J.-M. Buchlin, "Dynamics of gas jet impingement on vertical falling liquid films," in Proceedings of the 6th Symposium of VKI PhD Research, Rhode Saint Genese, 2015.
[11]Z. Wan, P. Wang, H. Shen, and Y. Li, "Falling film flow and heat transfer of cryogenic liquid oxygen on different structural surfaces," Energies **15**, 5040 (2022).
[12]Y. Zhou and J. Yu, "Optimization design of falling film type plate-fin condenser/reboilers by minimizing specific entropy generation rate," Cryogenics **99**, 25–31 (2019).
[13]Z. Dai, Y. Zhang, S. Wang, K. Nawaz, and A. Jacobi, "Falling-film heat exchangers used in desalination systems: A review," Int. J. Heat Mass Transfer **185**, 122407 (2022).
[14]H. Raach and J. Mitrovic, "Seawater falling film evaporation on vertical plates with turbulence wires," Desalination **183**, 307–316 (2005).
[15]E. Karlsson, M. Gourdon, L. Olausson, and L. Vamling, "Heat transfer for falling film evaporation of black liquor up to very high Prandtl numbers," Int. J. Heat Mass Transfer **65**, 907–918 (2013).
[16]P. Cyklis, "Effect of fouling on falling film evaporator performance in industrial conditions of fruit juice concentrate production," J. Food Eng. **317**, 110884 (2022).
[17]M. Gourdon, F. Innings, A. Jongsma, and L. Vamling, "Qualitative investigation of the flow behaviour during falling film evaporation of a dairy product," Exp. Therm. Fluid Sci. **60**, 9–19 (2015).
[18]H. Rößler, W. Wiesenhöfer, C. Glasmacher-Remberg, and C. Breucker, "Thin-film reactors," in *Ullmann's Encyclopedia of Industrial Chemistry* (Wiley-VCH, Weinheim, 2013).
[19]J. Villadsen and P. H. Nielsen, "Models for strongly exothermic absorption and reaction in falling films," Chem. Eng. Sci. **41**, 1655–1671 (1986).
[20]R. A. Havestini and S. J. Ormiston, "An elliptic numerical analysis of water vapour absorption into a falling film in vertical parallel plate channels," Int. J. Heat Mass Transfer **150**, 119266 (2020).
[21]M. Mortazavi, R. Nasr Isfahani, S. Bigham, and S. Moghaddam, "Absorption characteristics of falling film LiBr (lithium bromide) solution over a finned structure," Energy **87**, 270–278 (2015).
[22]T. F. O'Brien, "Salt, chlor-alkali, and related heavy chemicals," in *Handbook of Industrial Chemistry and Biotechnology*, edited by J. A. Kent, T. V. Bommaraju, and S. D. Barnicki (Springer International Publishing, Cham, 2017), pp. 1267–1300.
[23]D. Flagiello, F. Di Natale, A. Lancia, I. Sebastiani, F. Nava, A. Milicia, and A. Erto, "Experimental and modelling approach to the design of chemical absorption columns with fast gas-liquid reaction: A case-study on flue-gas desulfurization with H_2O_2 oxidative solutions," Chem. Eng. Res. Des. **194**, 425–438 (2023).
[24]P. Zhang, R. Chen, G. Su, W. Tian, and S. Qiu, "Experimental investigation and modeling of falling film heat transfer on partial dry-out condition," Appl. Therm. Eng. **229**, 120550 (2023).
[25]K. P. Akanksha and V. Srivastava, "Mass transport correlation for CO_2 absorption in aqueous monoethanolamine in a continuous film contactor," Chem. Eng. Process. **47**, 920–928 (2008).
[26]L. Broniarz-Press, "Enhancement of mass transfer coefficients in spiral films," Int. J. Heat Mass Transfer **40**, 4197–4208 (1997).
[27]N. Ghasem, "Efficient CO_2 absorption through wet and falling film membrane contactors: Insights from modeling and simulation," Sci. Rep. **13**, 10994 (2023).
[28]X. Luo, A. Hartono, and H. F. Svendsen, "Comparative kinetics of carbon dioxide absorption in unloaded aqueous monoethanolamine solutions using wetted wall and string of discs columns," Chem. Eng. Sci. **82**, 31–43 (2012).
[29]A. Maun, "Optimierung von Verfahren zur Kohlenstoffdioxid-Absorption aus Kraftwerksrauchgasen mithilfe alkalischer Carbonatlösungen," Ph.D. thesis (University of Duisburg-Essen, 2013).
[30]M. Zanfir, A. Gavriilidis, C. Wille, and V. Hessel, "Carbon dioxide absorption in a falling film microstructured reactor: Experiments and modeling," Ind. Eng. Chem. Res. **44**, 1742–1751 (2005).
[31]F. Zhang, L. Guo, Y. Ding, X. Zhu, and Q. Liao, "Flow pattern and CO_2 absorption in a falling film reactor with mixed aqueous solution of ionic liquid and MEA," Appl. Therm. Eng. **138**, 583–590 (2018).
[32]R. Bertling, M. Hack, I. Ausner, B. Horschitz, S. Bernemann, and E. Kenig, "Modelling film and rivulet flows on microstructured surfaces using CFD methods," Chem. Eng. Sci. **251**, 117414 (2022).
[33]Y. Haroun, L. Raynal, and P. Alix, "Prediction of effective area and liquid holdup in structured packings by CFD," Chem. Eng. Res. Des. **92**, 2247–2254 (2014).
[34]D. Sebastia-Saez, S. Gu, P. Ranganathan, and K. Papadikis, "Micro-scale CFD modeling of reactive mass transfer in falling liquid films within structured packing materials," Int. J. Greenhouse Gas Control **33**, 40–50 (2015).
[35]J. Davies and K. Warner, "The effect of large-scale roughness in promoting gas absorption," Chem. Eng. Sci. **24**, 231–240 (1969).
[36]V. Kapoustina, J. Guffart, A. Hien, J. Strischakov, I. Medina, M. Rädle, and J.-U. Repke, "Influence of a single microstructure on local mass transfer in liquid film flows," Chem. Eng. Res. Des. **146**, 352–362 (2019).
[37]M. Kohrt, I. Ausner, G. Wozny, and J.-U. Repke, "Texture influence on liquid-side mass transfer," Chem. Eng. Res. Des. **89**, 1405–1413 (2011).
[38]A. Åkesjö, M. Gourdon, L. Vamling, F. Innings, and S. Sasic, "Modified surfaces to enhance vertical falling film heat transfer – An experimental and numerical study," Int. J. Heat Mass Transfer **131**, 237–251 (2019).
[39]S. Chen, T. Zhang, L. Lv, Y. Chen, and S. Tang, "Simulation of the hydrodynamics and mass transfer in a falling film wavy microchannel," Chin. J. Chem. Eng. **34**, 97–105 (2021).
[40]H. Lu, L. Lu, and X. Gao, "Mass transfer enhancement of falling film liquid desiccant dehumidification by micro-baffle plates," Int. J. Heat Mass Transfer **169**, 120945 (2021).
[41]S. Negny, M. Meyer, and M. Prévost, "Modelling of the coupling hydrodynamic transfer for a gas–liquid countercurrent flow on a wavy surface," Chem. Eng. Sci. **58**, 2705–2714 (2003).
[42]L. Zhao and R. Cerro, "Experimental characterization of viscous film flows over complex surfaces," Int. J. Multiphase Flow **18**, 495–516 (1992).

[43]Y. Lu, F. Stehmann, S. Yuan, and S. Scholl, "Falling film on a vertical flat plate – Influence of liquid distribution and fluid properties on wetting behavior," Appl. Therm. Eng. **123**, 1386–1395 (2017).
[44]H. Ishikawa, S. Ookawara, S. Yoshikawa, and H. Matsumoto, "Numerical study on mass transfer in a falling film on structured plates with micro-baffles," Chem. Eng. Process. **175**, 108903 (2022).
[45]M. Kohrt, "Experimentelle Untersuchung von Stofftransport und Fluiddynamik bei Rieselfilmstromungen auf mikrostrukturierten Oberflächen," Ph.D. thesis (TU Berlin, 2012).
[46]S. Paschke, "Experimentelle Analyse ein- und zweiphasiger Filmströmungen auf glatten und strukturierten Oberflächen," Ph.D. thesis (TU Berlin, 2011).
[47]N. Aksel and M. Schörner, "Films over topography: From creeping flow to linear stability, theory, and experiments, a review," Acta Mech. **229**, 1453–1482 (2018).
[48]S. Kalliadasis, C. Bielarz, and G. M. Homsy, "Steady free-surface thin film flows over topography," Phys. Fluids **12**, 1889–1898 (2000).
[49]V. Bontozoglou and G. Papapolymerou, "Laminar film flow down a wavy incline," Int. J. Multiphase Flow **23**, 69–79 (1997).
[50]V. Bontozoglou and G. Papapolymerou, "Wall-triggered interfacial resonance in laminar gas-liquid flow," Int. J. Multiphase Flow **24**, 131–143 (1998).
[51]M. Pak and G. Hu, "Numerical investigations on vortical structures of viscous film flows along periodic rectangular corrugations," Int. J. Multiphase Flow **37**, 369–379 (2011).
[52]A. Wierschem, V. Bontozoglou, C. Heining, H. Uecker, and N. Aksel, "Linear resonance in viscous films on inclined wavy planes," Int. J. Multiphase Flow **34**, 580–589 (2008).
[53]M. Vlachogiannis and V. Bontozoglou, "Experiments on laminar film flow along a periodic wall," J. Fluid Mech. **457**, 133–156 (2002).
[54]K. Argyriadi, M. Vlachogiannis, and V. Bontozoglou, "Experimental study of inclined film flow along periodic corrugations: The effect of wall steepness," Phys. Fluids **18**, 012102 (2006).
[55]B. Al-Shamaa, T. Kahraman, and A. Wierschem, "Steady three-dimensional patterns in gravity-driven film flow down an inclined sinusoidal bottom contour," Phys. Fluids **35**, 033307 (2023).
[56]J. Wojtkowiak and C. O. Popiel, "Inherently linear annular-duct-type laminar flowmeter," J. Fluids Eng. **128**, 196–198 (2005).
[57]A. Schagen, "Methode der laser-induzierten Lumineszenz zur experimentellen Analyse des Stofftransportes in laminar-welligen Flüssigkeitsfilmen," Ph.D. thesis (RWTH Aachen University, 2014).
[58]N. Brauner and D. M. Maron, "Characteristics of inclined thin films, waviness and the associated mass transfer," Int. J. Heat Mass Transfer **25**, 99–110 (1982).
[59]Precitec, "Overview chromatic confocal point sensors," 2021, see https://www.precitec.com (last accessed December 12, 2022).
[60]A. A. Mouza, N. A. Vlachos, S. V. Paras, and A. J. Karabelas, "Measurement of liquid film thickness using a laser light absorption method," Exp. Fluids **28**, 355–359 (2000).
[61]W. Wagner and H.-J. Kretzschmar, "Wasser," in *VDI-Wärmeatlas* (Springer Verleg, Berlin, Heidelberg, 2013), pp. 175–195.
[62]F. Al-Sibai, "Experimentelle Untersuchung der Strömungscharakteristik und des Wärmeübergangs bei welligen Rieselfilmen," Ph.D. thesis (RWTH Aachen University, 2004).
[63]W. Nusselt, "Die Oberflächenkondensation des Wasserdampfes," Z. Ver. Dtsch. Ing. **60**, 541–546 (1916).
[64]H. Brauer, *Strömung und Wärmeübergang bei Rieselfilmen*, VDI-Forshungsheft Vol. 457 (VDI-Verlag, 1956).
[65]A. Ayati and J. Carneiro, "Statistical characterization of interfacial waves in turbulent stratified gas-liquid pipe flows," Int. J. Multiphase Flow **103**, 94–105 (2018).
[66]A. Fershtman, D. Barnea, and L. Shemer, "Wave identification in upward annular flow - A focus on ripple characterization," Int. J. Multiphase Flow **137**, 103560 (2021).
[67]D. Sebastia-Saez, S. Gu, P. Ranganathan, and K. Papadikis, "3D modeling of hydrodynamics and physical mass transfer characteristics of liquid film flows in structured packing elements," Int. J. Greenhouse Gas Control **19**, 492–502 (2013).
[68]M. Dauth and N. Aksel, "Breaking of waves on thin films over topographies," Phys. Fluids **30**, 082113 (2018).
[69]A. Wierschem and N. Aksel, "Hydraulic jumps and standing waves in gravity-driven flows of viscous liquids in wavy open channels," Phys. Fluids **16**, 3868–3877 (2004).
[70]M. Rietz, "Dynamics of falling films under the influence of a destabilizing body force," Ph.D. thesis (RWTH Aachen University, 2020).
[71]S. F. Kistler and L. E. Scriven, "The teapot effect: Sheet-forming flows with deflection, wetting and hysteresis," J. Fluid Mech. **263**, 19–62 (1994).
[72]A. Reitze, M. Grünewald, and J. Riese, "Concept of a flexible wetted-wall column for the distillation of specialty chemicals," Chem. Eng. Technol. **44**, 1327–1335 (2021).
[73]C. Heining, V. Bontozoglou, N. Aksel, and A. Wierschem, "Nonlinear resonance in viscous films on inclined wavy planes," Int. J. Multiphase Flow **35**, 78–90 (2009).
[74]Y. Guo, N. Liu, L. Cai, and W. Hong, "Experimental and numerical investigations of film flow behaviors in resonance section over corrugated plates," J. Zhejiang Univ., Sci., A **20**, 148–162 (2019).